Iridium Oxide Coordinatively Unsaturated Active Sites Govern the Electrocatalytic Oxidation of Water

Citation: J. J. Velasco Vélez, D. Bernsmeier, R. V. Mom, P. Zeller, Y. Shao-Horn, B. Roldan Cuenya, A. Knop-Gericke, R. Schlögl, T. E. Jones, Iridium Oxide Coordinatively Unsaturated Active Sites Govern the Electrocatalytic Oxidation of Water. Adv. Energy Mater. 2024, 2303407.

As Published: 10.1002/aenm.202303407

Publisher: Wiley

Persistent URL: https://hdl.handle.net/1721.1/154278

Version: Final published version: final published article, as it appeared in a journal, conference proceedings, or other formally published context

ADVANCED ENERGY MATERIALS
www.advenergymat.de

Iridium Oxide Coordinatively Unsaturated Active Sites Govern the Electrocatalytic Oxidation of Water

Juan Jesús Velasco Vélez, Denis Bernsmeier, Rik V. Mom, Patrick Zeller, Yang Shao-Horn, Beatriz Roldan Cuenya, Axel Knop-Gericke, Robert Schlögl, and Travis E. Jones**

A special membrane electrode assembly to measure *operando* X-ray absorption spectra and resonant photoemission spectra of mesoporous templated iridium oxide films is used. These films are calcined to different temperatures to mediate the catalyst activity. By combining *operando* resonant photoemission measurements of different films with ab initio simulations these are able to unambiguously distinguish μ_2-O (bridging oxygen) and μ_1-O (terminal oxygen) in the near-surface regions of the catalysts. The intrinsic activity of iridium oxide scales with the formation of μ_1-O (terminal oxygen) is found. Importantly, it is shown that the peroxo species do not accumulate under reaction conditions. Rather, the formation of μ_1-O species, which are active in O—O bond formation during the OER, is the most oxidized oxygen species observed, which is consistent with an O—O rate-limiting step. Thus, the oxygen species taking part in the electrochemical oxidation of water on iridium electrodes are more involved and complex than previously stated. This result highlights the importance of employing theory together with true and complementary *operando* measurements capable of probing different aspects of catalysts surfaces during operation.

1. Introduction

Hydrogen is both a critical commodity chemical and an attractive energy storage medium. It is also the most abundant element in the universe. However, hydrogen is rarely found as a pure gas; rather it requires separation from other elements.[1] In the earth, gaseous hydrogen can be found in underground reservoirs, so-called white hydrogen (or natural hydrogen).[2] Even if such hydrogen may be found in sufficiently localized quantities in the earth´s crust to make extraction economically feasible, identifying those locations and extracting the gas is still challenging. These facts lead to the need to produce H_2 gas through (electro)chemical means. Currently, most hydrogen is produced through steam reforming of fossil fuels,[3] which is a high-temperature process that produces

J. J. Velasco Vélez, A. Knop-Gericke, R. Schlögl
Department of Heterogeneous Reactions
Max Planck Institute for Chemical Energy Conversion
45470 Mülheim an der Ruhr, Germany
E-mail: jvelasco@cells.es

J. J. Velasco Vélez, R. V. Mom, P. Zeller, A. Knop-Gericke, R. Schlögl, T. E. Jones
Department of Inorganic Chemistry
Fritz-Haber-Institut der Max-Planck-Gesellschaft
14195 Berlin, Germany
E-mail: tejones@lanl.gov

J. J. Velasco Vélez
Experiments division
ALBA Synchrotron Light Source
Cerdanyola del Vallés, Barcelona 08290, Spain

D. Bernsmeier
Department of Chemistry
Chemical Engineering Division
Technical University Berlin
10623 Berlin, Germany

R. V. Mom
Leiden Institute of Chemistry
Leiden University
Leiden 2333 CC, The Netherlands

P. Zeller
Helmholtz-Zentrum Berlin für Materialen und Energie
12489 Berlin, Germany

Y. Shao-Horn
Department of Mechanical Engineering
Massachusetts Institute of Technology
Cambridge, MA 02139, USA

B. Roldan Cuenya
Department of Interface Science
Fritz-Haber-Institut der Max-Planck-Gesellschaft
14195 Berlin, Germany

T. E. Jones
Theoretical Division
Los Alamos National Laboratory
Los Alamos, NM 87545, USA

The ORCID identification number(s) for the author(s) of this article can be found under https://doi.org/10.1002/aenm.202303407

DOI: 10.1002/aenm.202303407

CO_2. For instance, a simple mass balance shows that methane steam reforming combined with water gas shift produces over 5.46 kg of CO_2 for each kg of H_2 produced, excluding the fuel cost associated with heating. Thus, steam reforming is not environmentally friendly as most of the CO_2 is released to the atmosphere contributing significantly to global warning. Such hydrogen produced from steam reforming is known as black or brown when coal is used as the hydrocarbon source and grey hydrogen when methane is used. If the greenhouse gases are captured, the produced hydrogen is known as blue hydrogen,[4] which typically involves methane steam reforming. A more environmentally friendly method is to produce hydrogen from water electrolysis. If the electrical energy needed for this reaction is supplied by a nuclear plant, the hydrogen produced is known as pink hydrogen. Meanwhile, if the electricity is produced from renewable sources of energy, the produced hydrogen is known as green hydrogen. Thus, green hydrogen technologies aim to facilitate the transition to a carbon-neutral economy.[5] However, water electrolysis is kinetically challenging,[6] and therefore requires high-performance catalysts, the mechanisms of which are the motivation of the present work.

In the water electrolysis two reactions take place simultaneously, one on each electrode. A catalyst on the cathode (usually platinum) facilitates the facile hydrogen evolution reaction (HER).[7] Meanwhile on the anode, the kinetically sluggish oxygen evolution reaction (OER) takes place, necessitating the use of potentials beyond the thermodynamic minimum, overpotentials, even with high-performance catalysts. Under acidic conditions and anodic potentials, the anode is also susceptible to severe corrosion that makes most of elements unsuitable for long-term use. Thus, the bottleneck in the production of green hydrogen is finding suitable catalysts for the OER due to the high overpotential and harsh operating conditions. Of all elements, iridium uniquely combines a low overpotential and high corrosion resistance under acidic conditions.[8,9] However, iridium is one of the scarcest elements in Earth´s crust. Widespread use of water electrolysis will then require strategies to optimize the use of iridium, which requires us to identify the electronic factors that make iridium unique in the OER.

The activity of iridium-based electrodes depends strongly on their physicochemical properties such as thickness,[10] crystallinity,[11] electrical conductivity, chemical composition,[12] and oxidation state. One strategy to reduce iridium loading is to employ porous materials,[13] which have high surface-to-bulk ratios as well as improved active site accessibility, making them an attractive OER electrodes.[14] However, while the OER performance of mesoporous IrO_x films is strongly influenced by accessible surface area and active sites per area,[13] the nature of the observed decreased activity after preparation at higher calcination temperatures is still unknown.[14] This change in activity is likely influenced by electronic structure and purely accessible area, like in the case of X-ray amorphous oxides.[15–17] A deeper understanding of the electronic factors making iridium unique in the electrocatalytic oxidation of water is then necessary to understand the performance of iridium(-hydr)oxide.[18] To achieve this goal, we must measure the electronic properties of IrO_x materials under *operando* conditions; that is, with the iridium in contact with electrolyte under potentiometric control.[19–22] To achieve these requirements, we produced a membrane electrode assembly (MEA) that allows the investigation of the electrode during *operando* conditions (i.e., measurements performed during electrocatalytic operation while simultaneously measuring the gas-phase products evolved during the reaction).[23] The fundamental understanding of iridium chemistry accessible through such measurements is necessary to produce electrodes based on abundant materials that are able to mimic iridium's electrocatalytic performance. Parameters such as chemical composition at the interface and electronic structure need to be known in order to accurately describe the mechanisms that take place under reaction conditions at the electrode/electrolyte interface during the OER. Furthermore, these data must be collected under *operando* conditions, which requires the determination of the evolved products (by a simultaneous product analytic technique) at the same time that the electronic structure and chemical composition are recorded with spectroscopic techniques.

To date, *operando* studies of the electronic structure of Ir-based OER catalysts have focused on X-ray photoelectron spectroscopy (XPS) and X-ray absorption spectroscopy (XAS) respectively.[10,19,20–22,24–32] Such studies have shown Ir oxidation states as high as Ir^V may be reached[10,26,28,30] during the OER. Moreover, XAS at the O K-edge has shown that at these high oxidation states, a variety of electron-deficient oxygen species form, including bridging μ_2-O bound to two iridium atoms and the terminal μ_1-O species bound to a single iridium atom.[20,22,24,25,26] Critical among these electron-deficient oxygen species (O^{I-}) is the μ_1-O oxyl bound to a single iridium atom, as it is thought to be active in the OER.[10,20,26] However, the unambiguous identification and assignment of a μ_1-O oxyl species is challenging with XAS alone because it appears as a low energy tail on the principal resonance at ≈529 eV excitation energy associated with the more abundant μ_2-O.[33,34] Furthermore, both the μ_1-OOH hydroperoxo and μ_1-OO peroxo, which are electron-deficient oxygen species that are argued to be thermodynamically stable under OER conditions,[35] are indistinguishable from other species in XAS at the O K-edge because their white lines at 532 eV excitation energy overlap with all other oxygen species.[15–18,20–22] Unambiguously identifying the appearance or absence of μ_1-O oxyl and μ_1-OO(H), and ultimately bounding their coverages, has major mechanistic implications since the former is thought to immediately precede O–O formation and the latter proceeds this possible slow step.[26]

While identifying and discriminating between the various electron-deficient oxygen species on iridium using XAS alone has proven impossible, resonant inelastic X-ray scattering (RIXS) can identify electron holes on oxygen due to a separation of the integrated XAS signal into spectra at fixed X-ray emission.[34] While such 2D spectral maps are useful in the identification of electron-deficient oxygen, RIXS is a bulk-sensitive technique that is not ideally suited to study surface chemistry. However, we can employ a similar strategy with resonant photoelectron spectroscopy (ResPES), where the O K-edge XA spectra are measured at fixed electron binding energy. This technique is element-specific, surface-sensitive, and is also extremely sensitive to changes in oxygen bonding,[36] as such, ResPES has been used to aid in the understanding of the electronic structure a variety of oxides, including identifying delocalized oxygen states in Ti oxides[37,38] and identifying defects in In[39] and Ga oxides.[40] A major advantage of ResPES is that, by separating

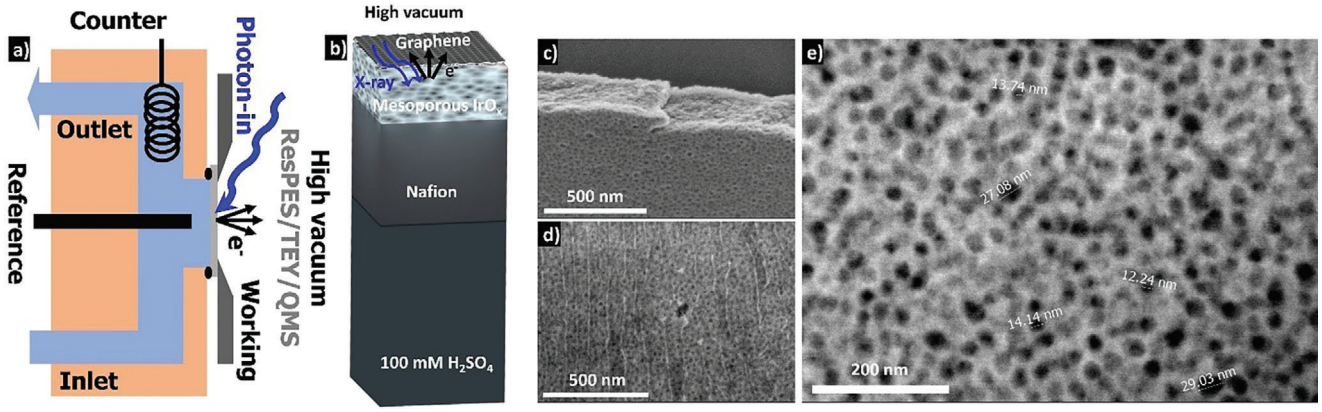

Figure 1. Schematic of a) the electrochemical cell used in these experiments and b) of the MEA and detection schemes used in this work. In this device, Nafion is wetted from the backside by electrolyte, and the electrolyte migrates through the Nafion to the mesoporous IrOx electrode. The working electrode is covered in a bilayer of graphene, which prevents the electrolyte from evaporating into the vacuum chamber while not obstructing incoming X-rays or outgoing photoelectrons. c) SEM image of the mesoporous thin film calcined at 375 °C, including the surface and cross-section. d) SEM overview picture of the MEA in c with the IrOx mesoporous coated with a bilayer of graphene (note that the wrinkles observed are a consequence of transferring the graphene onto the mesoporous IrOx surface). e) SEM micrograph showing the pore size distribution of the mesoporous film shown in c) and d).

binding and excitation energies, it may allow full speciation of the active surface by, for instance, separating the μ_2-O and μ_1-O species from each other along the binding energy axis while separating them from other oxygen species along the excitation energy axis, or similarly for separating μ_1-OO(H) from other oxygen species.

To take advantage of these favorable aspects of ResPES, we have developed a unique advanced capabilities in *operando* ResPES to allow speciation by simultaneously resolving spectra in binding and excitation energy while also achieving extreme surface sensitivity and element specificity. We combine the simultaneous collection of X-ray photoelectron spectra with quadrupole mass spectrometry (QMS) to determine the interface electronic structure at the same time that the evolved products are measured (mostly O_2 in the present case). Thus, while the atomistic description of the working catalyst cannot be concluded from ex situ characterization, as the measured reaction intermediates are formed under *operando* conditions, combining ResPES with ab initio calculations allows us to identify several oxygenated iridium species that appear under *operando* conditions. These results indicate the OER is more complex than is typically assumed. More specifically, the IrO_x calcined at lower temperatures are more active due to their ability to produce low coordinate, terminal μ_1-O and bridging μ_2-O, oxygen species that facilitate the formation of O_2 gas.

2. Experimental Section

2.1. Membrane Electrode Assembly (MEA) Fabrication

A schematic drawing of the electrochemical cell used in these experiments is shown in **Figure** 1a. A scheme for the membrane electrode assembly (MEA) preparation and photoelectron collection is shown in Figure 1b. The hemispherical analyzer is located in the high vacuum chamber. The mesoporous IrO_x film was prepared by iridium acetate and micelles of amphiphilic block-copolymers using an evaporation-induced self-assembly (EISA) method,[13] where the pore size is accurately controlled by the triblock copolymer. Silicon wafers were coated with iridium oxide films via dip-coating by first cleaning the wafer with C_2H_6O. The silicon wafer was then dip-coated in a solution formed by adding 450 mg of $C_{14}H_{27}Ir_3O_{20}$ and 90 mg of a polymer template $CH_3O(C_2H_4O)_m(C_4H_8O)_nH$ (containing 18 700 g mol^{-1} $C_{2n}H_{4n+2}O_{n+1}$ and 10 000 g mol^{-1} $(C_4H_8)_n$ sourced from Polymer service Merseburg GmbH) to a volume of 3 mL of C_2H_6O. The dip coating process was performed at a temperature of 25 °C and a relative humidity of 40% in a controlled atmosphere using a withdrawal rate of 200 mm min^{-1}. The film deposited on the silicon wafer was transferred immediately to a preheated muffle furnace in a continuous flowing air atmosphere, where it remained for 5 min. For the current study the films were prepared at two different temperatures 375 °C and 500 °C yielding different crystallinity and pore structure for these two mesoporous films, as well as different reactivities (see Figure 1c–e). The scannin electron microscopy (SEM) images reveal an average pore size of 20 nm with a distance between pores of ~30 nm and a catalyst film thickness of 100 nm. The films grown by the EISA method were transferred to a Nafion 115 membrane (sourced by Sigma–Aldrich) by hot pressing the ionomeric membrane to the surface of the mesoporous IrO_x at 80 °C and pulling it back off the wafer. The hot press transfer approach yields a homogenous mesoporous film on the surface of the ionomeric membrane.

The mesoporous IrO_x film was finally sandwiched between the Nafion membrane and bi-layered graphene (BLG).[41] The BLG, grown on a 20 µm thick copper foil by chemical vapor deposition (CVD), was purchased from Graphenea (Spain). The copper support was dissolved by floating the supported BLG on a 50 mM aqueous solution of $(NH_4)_2S_2O_8$ before rinsing in DI-water. The BLG layer was transferred onto the mesoporous IrO_x/Nafion as shown schematically in Figure 1b. The BLG-covered mesoporous IrO_x is shown in Figure 1c,d, where the graphene wrinkles in the surface can be observed. Preparing the MEA in this way allows the graphene layer to

function as a water evaporation barrier (forming a confined liquid between the Nafion and graphene), and current collector. Critically, since the BLG is transparent to the photoelectrons, this type of MEA allows us to perform *operando* photoelectron spectroscopy to characterize the electrode-electrolyte interface.[23]

2.2. Operando Electrochemical Cell

The main body of the electrochemical cell (EC-cell) is made of polyether ether ketone (PEEK), which is an excellent electrical insulator and chemically inert.[42–44] The electrolyte that flows in the cell is sealed using Kalrez O-rings. The EC-cell has three electrodes: a reference electrode (Ag/AgCl DRIREF-2SH, World Precision Instruments, USA), a counter platinum electrode, and the working electrode. In this study, the working electrodes were each one of the MEAs previously described (note, that the MEA is held in place using a boron dope diamond lid). All reported potentials were corrected to a reversible hydrogen electrode (RHE) using $V_{RHE} = V_{Ag/AgCl} + 0.254$ V (with pH 1 for this work) and are reported without *i*R compensation. The EC-cell is operated in the main chamber of the AP-XPS endstation of the ISISS beamline in BESSY II (Berlin, Germany) at a background pressure of $\sim 10^{-6}$ mbar during operation while aqueous electrolyte (0.1 M H_2SO_4 bubbled with N_2) is flowed at 1 ml min^{-1}. The electrolyte is back filled using a continuous flow with a peristaltic pump (PERIMAX 16-Antipuls from SPETEC), which allows for optimal membrane hydration and gas bubble elimination. The MEA assembly faces the vacuum chamber, where the X-rays are sourced and the photoelectrons are collected using the hemispherical analyzer to measure ResPES or a Faraday cup to collect the total electron yield (TEY) XAS.

2.3. Beamlines

The *operando* measurements were collected in the ambient pressure X-ray photoelectron spectrometer (AP-XPS) end-station of the ISISS beamline, which is a SPECS PHOIBOS 150 NAP. The *operand*-based experiments were done at the ISISS beamline of BESSY II in Berlin (Germany). The photons are sourced from a bending magnet (D41) and a plane grating monochromator (PGM) yielding an energy range from 80 to 2000 eV (soft X-ray range), a flux of 6×10^{10} photons/s with 0.1 A ring current using a 111 μm slit and an 80 μm × 200 μm beamspot size.

2.4. Electrolyte Preparation

The electrolyte was prepared by diluting 9.8 g of H_2SO_4 (purity 98%, Alfa Aesar, Massachusetts, USA) in 1 L of Milli-Q water (18.2 MΩ) at room temperature (RT), 25 °C, to achieve a pH of ≈1. The electrolyte was deareated by bubbling it with pure N_2 gas.

2.5. Potentiostat

A Biologic SP-300 (Seyssinet-Pariset, France) potentiostat was used for the experiments.

2.6. Calculations

All density functional theory (DFT) calculations were performed with the Quantum ESPRESSO package[45,46] using Perdew Burke Ernzerhof exchange and correlation potential (PBE)[47] with projector augmented wave (PAW) datasets from the PS library.[48] A kinetic energy cutoff of 60 Ry and a charge density cutoff of 600 Ry were used. To model rutile-type IrO_2 surfaces (110) terminated 8-layer slabs and (111) terminated 10-layer slabs separated by *c.a.* 15 Å of vacuum was employed. During ionic relaxation, the central 2-layer were fixed to their bulk positions. A ***k***-point mesh equivalent to (6 × 3) for the (1 × 1) (110) surface unit cell and (6 × 6) for the (1 × 1) (111) surface unit cell together with cold smearing with a smearing parameter of 0.01 Ry was employed. O K-edge spectra were computed by solving the Bethe–Salpeter Equation (BSE) using the ground state wavefunctions from Quantum ESPRESSO with the NSIT core-level BSE solver[49,50] through the OCEAN package.[51] For this purpose, wavefunctions were computed using norm-conserving pseudopotentials with a kinetic energy cutoff of 120 Ry including states to over 100 eV above the Fermi energy. The energy alignment of the O Kedge was performed by of ΔSCF[52] calculations using Quantum ESPRESSO, where a simulation on (4 × 4 × 4) bulk IrO_2 was used to align to experiment. The Auger spectra were computed using the Cini-Sawatzky theory where the impurity density of states was computed using Quantum ESPRESSO.[53] In all cases a U_{pp} of 2 eV was employed. ResPES maps were constructed by plotting the product of the resonant Auger contribution to the valence band and the XA spectra across an excitation energy window spanning 527–534 eV and a binding energy window spanning 0–25 eV.

3. Results and Discussion

The electronic structure of the IrO_x mesoporous films were investigated using XAS at the O K-edge X-ray, or simply O K-edge spectra. The O K-edge probes electronic transition from the occupied O 1s orbital to the unoccupied O 2p states that are hybridized with the Ir 5d states. The bulk rutile-type IrO_2 O K-edge spectrum has two features at ≈530 and ≈533 eV ascribed to hybridization of O 2p and Ir 5d orbitals of nominally t_{2g} and e_g symmetry, that is π^* and σ^* antibonding states,[45] respectively. Meanwhile, amorphous IrO_x shows a prominent peak at around ~529 eV (**Figure 2b**), which can be attributed to electron-deficient O^{I-} species.[15,16] This resonance is also seen in the mesoporous IrO_x, where their intensity depends on the calcination temperature as shown in Figure 2a. XAS at the O-K edge has revealed the species at ≈529 eV attributed to electron-deficient species (O^{I-}) may participate in the O–O bond formation during the OER.[20] Such electron-deficient species (O^{I-}) are more likely present in amorphous IrO_x under vacuum than on rutile-type IrO_2,[15–17] as shown in the reference spectra in Figure 2b. Moreover, O^{I-} forms on amorphous-type IrO_x under *operando* conditions, and such oxygen-rich stoichiometries may be essential for the OER on iridium electrodes.[10,20,25]

To investigate if the O^{I-} generated during the OER is responsible for the high activity of mesoporous IrO_x and if the surface chemistry also involves (hydro)peroxo species, like those suggested to participate in OER,[54] or result in surface instability,[35]

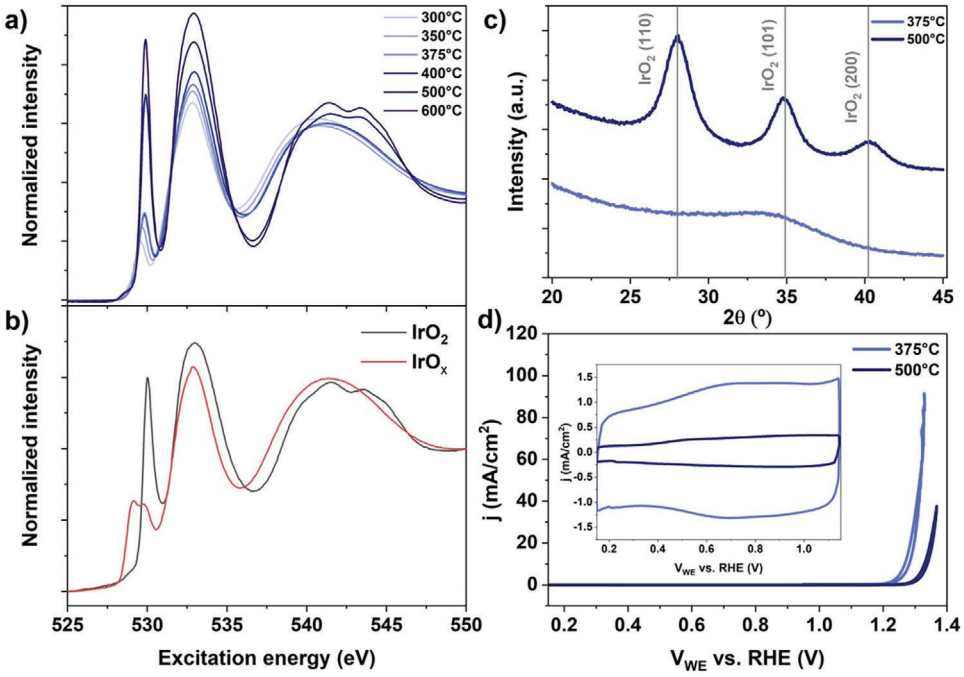

Figure 2. a) O K-edge TEY-XAS measurements of mesoporous IrO_x calcinated at different temperatures, as indicated. b) O K-edge TEY-XAS measurements of rutile-type IrO_2 and amorphous IrO_x reference samples. c) XRD measurements of the sample deposited on a Si wafer and calcined for 5 min at 500 and 375 °C. d) Electrocatalytic activity (in 0.5 H_2SO_4) of mesoporous IrO_x films deposited on Ti current collector calcined for 5 min at 500 and 375 °C in oxygen evolution reaction (OER) and electrochemical surface area (ECSA) regime (inset).

operando experiments were performed. The sample used for these experiments (from the panel of samples templated at different temperatures, Figure 2a) was the sample calcinated at 375 °C. This sample is amorphous compared the sample calcined at 375 °C temperature, Figure 2c. We selected the sample prepared at 375°C for *operando* characterization with XAS due to its higher activity compared to the samples templated at higher temperatures (Figure 2d). **Figure 3** shows the *operando* experiments performed with XAS in TEY mode. The electrocatalytic performance is shown in Figure 3b,c (current) (applied potential), where the different chronoamperometry (CA) measurements were collected in 100 mM H_2SO_4 (de-aerated in N_2). At potentials below +1.054 V versus RHE, there is no significant faradaic current and no evolution of O_2 as shown by the on-line QMS measurements ($m/z = 32$), where there is no observable change ascribed to the formation of any extra resonances at the O K-edge. However, at +1.454 V versus RHE potential (and higher) there is a noticeable increase in the faradaic current, which is ascribed to the evolution of O_2 as seen in the on-line QMS measurements. Under these conditions, the *operando* TEY-XAS measurements show the formation of O_2 (the resonance at ~530.2 eV), as well as the formation of a peak at ~528.0 eV ascribed to the formation of an electron-deficient O^{I-} species,[15–17] which are believed to be the active species and/or key intermediates/promoters in the reaction pathway.[10,20,25,26] However, the peak at 528.0 eV does not increase appreciably when the potential exceeds +1.854 V

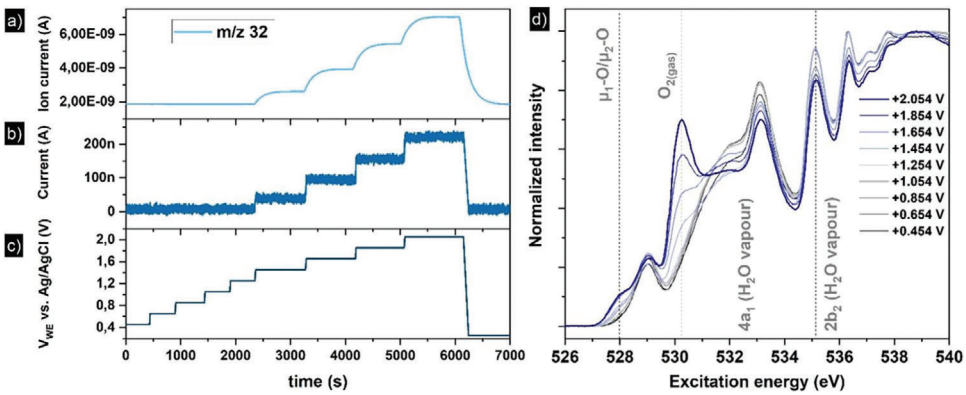

Figure 3. *Operando* characterization of the MEA using IrOx calcined at 375 °C: a) QMS measurements of $m/z = 32$ and b) current at the working electrode potential versus RHE shown in c). d) O K-edge TEY measurements at the electrode potentials shown in c).

versus RHE (without *i*R compensation). This fact can be ascribed to the surface approaching a limiting coverage of electron-deficient O^{I-} species,[15–17] where the increase in O_2 production beyond +1.854 V versus RHE is driven by an increase in the activity of electron deficient oxygen species rather than a large increase in number of these species. Remarkably, the results shown here are a clear example of true *operando* measurements where the physicochemical changes can be correlated directly, i.e., faradaic current can be correlated with evolved products and changes electronic structure while the sample is under potential control.

The assignment of electron-deficient oxygen may, however, be more involved than previously assumed[18] because different species have resonances at ≈528 eV during the OER. XAS alone is not able to determine the different species formed during the OER due to the overlapping of several oxygen species at similar excitation energies (within the lifetime and experimental broadening).[22] Specially, oxygen atoms bound to three iridium atoms (μ_3-O) can be distinguished from oxygen singly (μ_1-O) and doubly (μ_2-O) coordinated to iridium. Thus, while potentiodynamic XAS shows the existence of different species at ≈528 eV,[22] the speciation between μ_1-O and μ_2-O is non-trivial due to their similar excitation energies and peak broadening. By discriminating intensity in both excitation and binding energies, *operando* ResPES offers a means of disentangling these species.

In order to aid in speciation through ResPES, two different samples were prepared at two different temperatures, 500 and 375 °C. Since the activity depends on the preparation temperature, the samples prepared at high temperature are less active.[14] Thus, the resulting activity and stability depends strongly on the oxide composition and the synthesis approach (i.e., calcination temperature in this study). The samples calcined at 500 and 375 °C were investigated using ResPES at open circuit potential (OCP) and under OER conditions. ResPES was collected by sweeping the excitation energy across the O 1s core level while collecting photoelectrons with a binding energy of 0–25 eV. That is, valence band photoemission spectra were measured as the photon energy was scanned across the O 1s absorption threshold. Using excitation energies near the O 1s threshold results in resonant enhancement of oxygen features in the valence band. Thus, O 1s ResPES yields spectra that are particularly informative about the electronic structure of oxygen.[23,36–40] Specifically, O 1s ResPES maps yield simultaneous information about the occupied and unoccupied projected density of states (PDOS) together with the resonant Auger spectra of oxygen. By simultaneously measuring the valence band (VB) and XA spectra, however, the PDOS and resonant Auger spectra are measured as a function of excitation energy. ResPES then opens the possibility for improved speciation of the oxygen involved in the OER since the photoelectron intensity is resolved as a function of the excitation energy and binding energy to yield 2D maps, which allows us to disentangle species at similar excitation energies in the XA spectra.

Figure 4 shows the *operando* ResPES measurements collected for the electrodes prepared at 500 and 375 °C under OCP and OER conditions. The sample prepared at 375 °C shows a strong resonant peak at 529.0 eV excitation energy (EE) and 15.8 eV binding energy (BE) under OCP conditions (Figure 4c). Under OER conditions, the ResPES map shows the formation of new resonant peaks at (530 eV EE, 13.0 eV BE), and (528.0 eV EE, 13.4 eV BE) (Figure 4d), as well as an extra peak at (528.9 eV EE, 8.8 eV BE). On the other hand, the sample prepared a 500 °C has a peak at (529.5 eV EE, 16.4 eV BE) under OCP conditions; under OER conditions this sample does not show significant changes in the ResPES map (i.e., no new peaks emerge), as shown in Figure 4a,b, respectively. These results suggest that the electrodes prepared at 500 °C are not able to produce as many active species during the OER as the electrodes calcined at 375 °C, which is consistent with the lower activity of the electrodes calcined at 500 °C (Figure 2d) compared to the electrodes produced at lower temperatures. Thus, the electrodes fabricated at lower temperatures show a higher density of electron-deficient oxygen than the more crystallized samples prepared at higher temperatures.

To identify the oxygen species active in the OER revealed by the *operando* characterization, the ResPES spectra for different oxygen species on the surface of Ir were calculated using DFT combined with Cini–Sawatsky theory, while the XA spectra were computed at the BSE level. **Figure 5** shows the computed ResPES maps for μ_3-O, μ_2-O, μ_1-O and μ_1-OO.

Figure 6a shows the resonant Auger, or constant EE slices, associated with μ_3-O, μ_2-OH, μ_2-O, μ_1-OH, μ_1-O, and μ_1-OOH, and μ_1-OO on the (110) and (111) surfaces compared to the constant EE slices at the corresponding energies taken from experiment, that is, ≈ 530 eV for the μ_3-O and μ_2-OH, 529 eV for the μ_2-O and μ_1-OH, 528 eV for the μ_1-O, and 532 eV for the μ_1-OOH and μ_1-OO. In both the maps and constant EE slices, the μ_3-O species contributes at (530 eV EE, and 17.5 eV BE) and can account for the main Auger peak in all measured spectra. The ResPES peak that grows in for the sample prepared at 375 °C under OER conditions (Figure 6c) at (529.0 eV EE, 15.8 eV BE) can be assigned to μ_2-O, while that at (528.0 eV EE, 13.4 eV BE) can be attributed to μ_1-O. While the less active sample prepared at 500 °C appears to have some μ_2-O intensity, it lacks intensity in the region associated with μ_1-O, consistent with this oxyl species being active in the OER.[10,20,26] Moreover, we are now able to address (hydro)peroxo species directly. Peroxo and hydroperoxo appear at 532 eV in the O K-edge, making them indistinguishable from other species in XAS alone, as can be seen by the strong contribution at 532 eV under OCP conditions. From the simulations, Figure 5 and Figure 6, (hydro)peroxo species can be identified by a unique combination of high EE and low BE, (532 eV EE, 12 eV BE) and (532 eV EE, 6 eV BE). The absence of these features from the ResPES maps (Figure 4b,d) in both materials suggests (hydro)peroxo species are not present in significant amounts, which is in line with the OER being kinetically limited by O–O bond formation and further supported by in situ Raman measurements.[55]

To understand the nature of the active surfaces, consider that the μ_3-O shows a resonant peak at the energy ≈ (530 eV EE, 17 eV BE), meanwhile μ_2-O at (529 eV EE, 13 eV BE) and μ_1-O at (528 eV EE, 13 eV BE), respectively, see Figure 5. The (hydro)peroxo μ_1-OO species has characteristic resonant peaks at (532 eV EE, 12 and 6 eV BE). The sample prepared at 500 °C has a dominant species under OCP conditions at (529.5 eV EE, 16.4 eV BE), which is ascribed to the presence of μ_3-O. In addition, under OER conditions, the sample prepared at 500 °C doesn´t show the formation of μ_1-O and only limited μ_2-O species. Thus, this more crystalline iridium oxide surface is rich in μ_3-O, which are inactive in O–O bond formation.

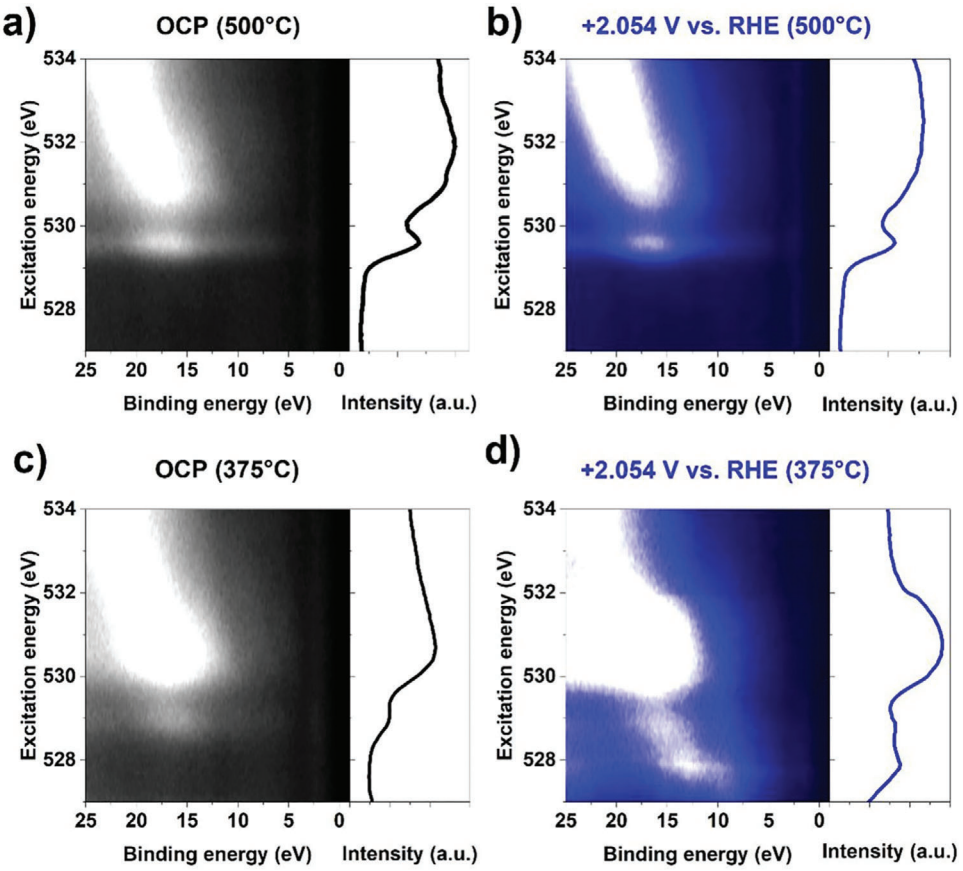

Figure 4. ResPES maps measured with photon energies in the vicinity of the O 1s core level by scanning the excitation energy through the O K-edge for the sample prepared at 500 °C under a) OCP and b) OER conditions and for the sample prepared at 375 °C under c) OCP and d) OER conditions.

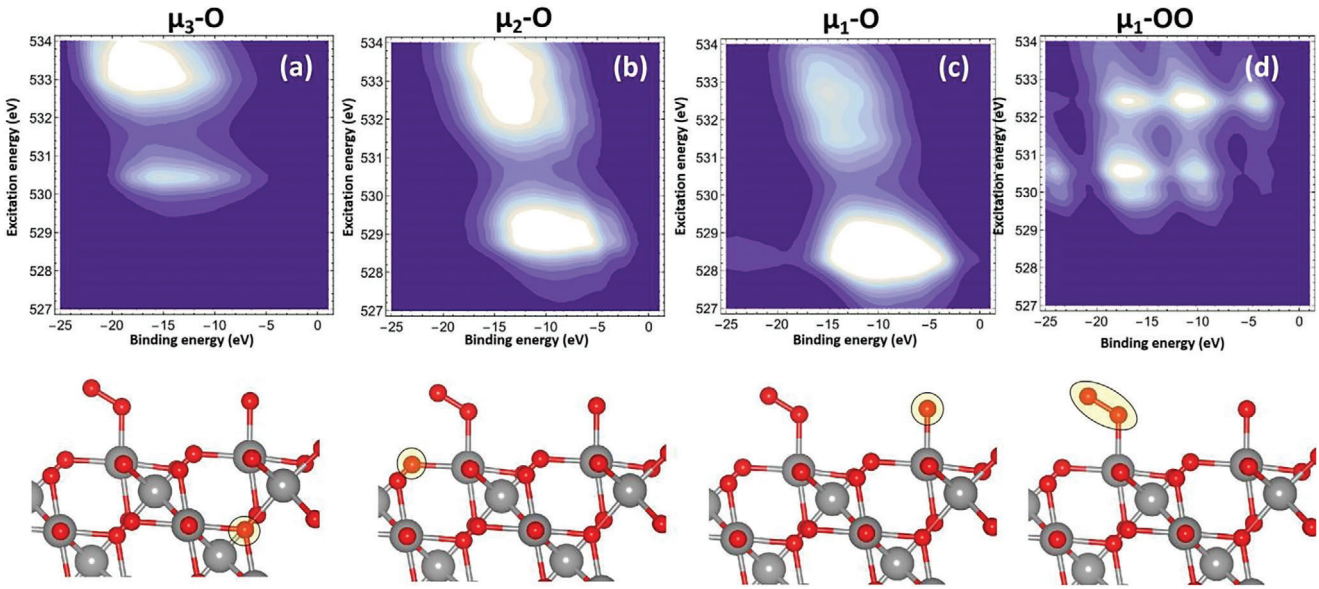

Figure 5. Calculated ResPES maps using photon energies in the vicinity of the O 1s core level. The excitation energy spans across the O K-edge absorption threshold while the binding energy is constrained to the valence band region. The intensity in the maps shows the resonant Auger contribution for: a) μ_3-O, b) μ_2-O, c) μ_1-O, and d) μ_1-OO, where the ball and stick models indicate the atomic structure on the (111) surface of rutile-type IrO_2.

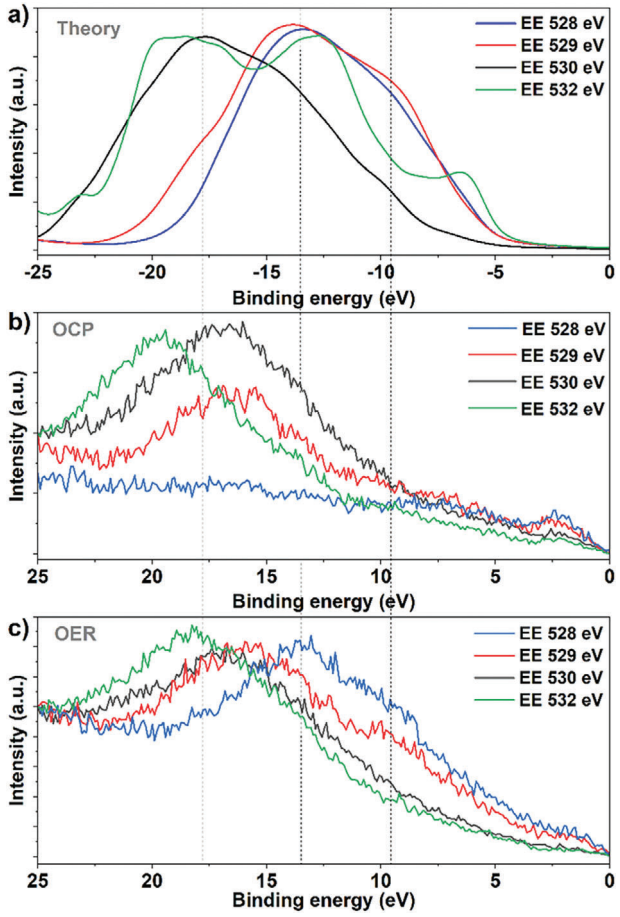

Figure 6. a) Calculated resonant Auger spectra of oxygen species on the (110) and (111) surfaces of rutile-type IrO_2. The computed EE of the various species are ≈ 530 eV for the μ_3-O and μ_2-OH, 529 eV for the μ_2-O and μ_1-OH, 528 eV for the μ_1-O, and 532 eV for the μ_1-OOH and μ_1-OO. Measured spectra under b) OCP and c) OER conditions.

On the other hand, the ResPES maps for the sample prepared at 375 °C shows a mixed-state with μ_3-O and μ_2-O species under OCP, in good agreement with the *operando* measurements (Figure 4c) and simulations (Figure 5b,c), indicating that the surfaces of these electrodes are rich in μ_2-O. Under OER the interpretation of the *operando* ResPES is more complex, with the simulations showing μ_1-O forms during the reaction. However, there is no evidence for the accumulation of μ_1-OO(H). Consequently, the *operando* ResPES map measured at 2.054 V versus RHE (Figure 4d), resembles the calculated ResPES map containing 1 monolayer (ML) μ_3-O together with fractional coverages of μ_2-O and μ_1-O (1/2 ML and 1/10 ML, respectively), **Figure** 7. Note that the coverages of the oxidized species (μ_2-O and μ_1-O) increase with potential,[22,26] nearly plateauing at 1.854 V versus RHE. These results indicate that a surface rich in coordination defects is more active and is able to produce more active species than a crystalline material. These results also highlight that there are different types of oxygen species present simultaneously during the OER but not all of them participate in the reaction, and only some facilitate it. At this point it is also important to remark that the XAS resonance assigned to O^{I-} species formed during the OER includes both bridging (μ_2-O) and terminal (μ_1-O) oxygen atoms, only the later are the oxyl species active in the OER,[10,26] however the precise electronic structure of these species varies between different iridium (hydr-)oxides.

According to these results, there are different oxygen species present in the near-surface region of the iridium oxide electrode during the OER but not all of them are directly involved in the production of dioxygen. The numbers of oxygen atoms singly (μ_1-O) and doubly coordinated (μ_2-O) to iridium might determine the activity of the sample during the OER. Such species are present on all surfaces, but are more abundant in defective oxides as indicated by their correlation with crystallinity.[11] This observation explains the enhanced activity of the defective materials. Here we highlight the μ_1-O (active) and μ_2-O (inactive) species, which correspond to the XAS peak at ≈528-529 eV in the O K-edge, where the presence of the two species is confirmed with ResPES. The peak at ≈528 eV becomes more intense with increasing potential until it reaches a plateau at sub-monolayer coverages of μ_1-O and μ_2-O (see Figure 3), with μ_1-O coverage being significantly less than μ_2-O or μ_3-O. Similarly, with the ability of ResPES to distinguish (hydro)peroxo species from the background we were able to show the μ_1-OO(H) species favored at OER potentials[35] are not present in a detectable coverage (<<1/10 ML) on an electrode operating as high as 2.054 V versus RHE.

4. Conclusion

Independent of the spectroscopic methodology employed, a resonance at ≈529 eV appears in the O K-edge XA spectrum of Ir-based electrodes under OER conditions, which is ascribed to electron-deficient oxygen species. However, using an advanced MEA preparation together with *operando* ResPES measurements and ab initio calculations, we were able to show that at potentials as high as 2.054 V versus RHE this peak contains contributions from two different species, namely μ_2-O (bridging oxygen) and μ_1-O (terminal oxygen). The coverage of these oxidized species was found to increase with potential, with the μ_1-O reaching up to ≈1/10 ML at 2.054 V versus RHE. In addition, the μ_1-OO (peroxo) and μ_1-OOH (hydroperoxo) species predicted to be the dominant species within the computational hydrogen electrode methodology, do not accumulate beyond <<1/10 ML under OER conditions. These results indicate the surface coverages of oxygen species are controlled by the kinetics of slow O—O

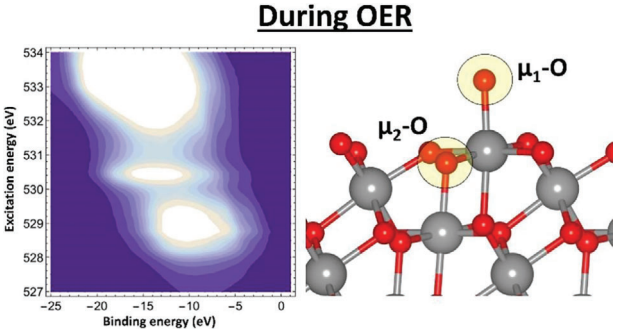

Figure 7. Calculated ResPES maps using photon energies in the vicinity of the O 1s core level for a surface with 1 ML μ_3-O, ½ ML μ_2-O, and 1/10 ML μ_1-O.

bond formation. We conclude that this result is of prime importance and represents a substantial advance in the understanding of the complex OER on IrO_x electrodes. Furthermore, this work highlights the importance of combining advance preparation, *operando* characterization ab initio calculations when studying the kinetics of surface reactions.

Acknowledgements

Helmholtz Zentrum Berlin für Materialien und Energie for allocating beamtime for the experiments within the proposal numbers 192–08521 and 191–08014. TEJ acknowledges support from the Laboratory Directed Research and Development program of Los Alamos National Laboratory under project number 20240061 DR.

Conflict of Interest

The authors declare no conflict of interest.

Data Availability Statement

The data that support the findings of this study are available from the corresponding author upon reasonable request.

Keywords

density functional theory, iridium oxide, membrane electrode assembling, operando X-ray photoelectron spectroscopy, oxygen evolution reaction

Received: October 9, 2023
Revised: December 26, 2023
Published online:

[1] N. Armaroli, V. Balzani, *ChemSusChem* **2011**, *4*, 21.
[2] V. Zgonnik, *Earth-Sci. Rev.* **2020**, *203*, 103140.
[3] D. R. Palo, R. A. Dagle, J. D. Holladay, *Chem. Rev.* **2007**, *107*, 3992.
[4] T. M. Gür, *J..Electrochem. Soc.* **2021**, *168*, 114516.
[5] R. Schlögl, *Ang. Chem. Int. Ed.* **2017**, *56*, 11019.
[6] M. G. Walter, E. L. Warren, J. R. McKone, S. W. Boettcher, Q. Mi, E. A. Santori, N. S. Lewis, *Chem. Rev.* **2010**, *110*, 6446.
[7] I. T. McCrum, M. T. Koper, *Nat. Ener.* **2020**, *5*, 891.
[8] Y. Lee, J. Suntivich, K. J. May, E. E. Perry, Y. Shao-Horn, *J. Phys. Chem. Lett.* **2012**,*3*, 399.
[9] T. C. Wen, C. C. Hu, *J. Electrochem. Soc.* **1992**, *139*, 2158.
[10] J. J. Velasco-Vélez, E. A. Carbonio, C. H. Chuang, C. J. Hsu, J. F. Lee, R. Arrigo, T. Jones, *J. American Chem. Soc.* **2021**, *143*, 12524.
[11] N. Deka, T. E. Jones, L. J. Falling, L. E. Sandoval-Diaz, T. Lunkenbein, J. J. Velasco-Velez, J. J., R. V. Mom, *ACS Cat.* **2023**, *13*, 7488.
[12] C. Spöri, P. Briois, H. N. Nong, T. Reier, A. Billard, S. Kühl, P. Strasser, *ACS Cat.* **2019**, *9*, 6653.
[13] E. Ortel, T. Reier, P. Strasser, R. Kraehnert, *Chem. Mat.* **2011**, *23*, 3201.
[14] R. Sachse, M. Pflüger, J. J. Velasco-Vélez, M. Sahre, J. Radnik, M. Bernicke, A. Hertwig, *ACS Cat.* **2020**, *10*, 14210.
[15] V. Pfeifer, T. E. Jones, J. J. Velasco Vélez, C. Massué, R. Arrigo, D. Teschner, R. Schlögl, *Surf. Inter. Anal.* **2016**, *48*, 261.
[16] V. Pfeifer, T. E. Jones, J. V. Vélez, C. Massué, M. T. Greiner, R. Arrigo, R. Schlögl, *Phys. Chem. Chem. Phys.* **2016**, *18*, 2292.
[17] V. Pfeifer, T. E. Jones, S. Wrabetz, C. Massué, J. J. V. Vélez, R. Arrigo, R. Schlögl, *Chem. Sci.* **2016**, *7*, 6791.
[18] L. J. Falling, J. J. Velasco-Vélez, R. V. Mom, A. Knop-Gericke, R. Schlögl, D. Teschner, T. E. Jones, *Curr. Op. Electrochem.* **2021**, *30*, 100842.
[19] H. G. Sanchez Casalongue, M. L. Ng, S. Kaya, D. Friebel, H. Ogasawara, A. Nilsson, *Ang. Chem. Int. Ed.* **2014**, *53*, 7169.
[20] V. Pfeifer, T. E. Jones, J. J. V. Vélez, R. Arrigo, S. Piccinin, M. Hävecker, R. Schlögl, *Chem. Sci.* **2017**, *8*, 2143.
[21] J. J. Velasco-Vélez, T. E. Jones, V. Streibel, M. Hävecker, C. H. Chuang, L. Frevel, A. Knop-Gericke, *Surf. Sci.* **2019**, *681*, 1.
[22] L. J. Frevel, R. Mom, J. J. Velasco-Vélez, M. Plodinec, A. Knop-Gericke, R. Schlögl, T. E. Jones, *J. Phys. Chem. C* **2019**, *123*, 9146.
[23] J. J. V. Vélez, D. Bernsmeier, T. E. Jones, P. Zeller, E. Carbonio, C. H. Chuang, R. Schlögl, *Farad. Dis.* **2022**, *236*, 103.
[24] R. V. Mom, L. J. Falling, O. Kasian, G. Algara-Siller, D. Teschner, R. H. Crabtree, A. Knop-Gericke, K. J. J. Mayrhofer, J. J. Velasco-Vélez, T. E. Jones, *ACS Catal.* **2022**, *12*, 5174.
[25] V. A. Saveleva, L. Wang, D. Teschner, T. Jones, A. S. Gago, A. Friedrich, S. Zafeiratos, R. Schlögl, E. R. Savinova, *J. Phys. Chem. Lett.* **2018**, *9*, 3154.
[26] H. N. Nong, L. J. Falling, A. Bergmann, M. Klingenhof, H. P. Tran, C. Spöri, R. Mom, J. Timoshenko, G. Zichitella, a. knop-Gericke, S. Piccini, J. Pérez-Ramírez, B. Roldan Cuenya, R. Schlögl, P. Strasser, D. Teschner, T. E. Jones, *Nature* **2020**, *587*, 408.
[27] S. Czioska, A. Boubnov, D. Escalera-López, J. Geppert, A. Zagalskaya, P. Röse, E. Saraçi, V. Alexandrov, U. Krewer, S. Cherevko, J. D. Grunwaldt, *ACS Catal.* **2021**, *11*, 10043.
[28] A. Minguzzi, C. Locatelli, O. Lugaresi, E. Achilli, G. Cappalletti, M. Scavini, M. Coduri, P. Masala, B. Sacchi, A. Vertova, P. Ghigna, S. Rondinini, *ACS Catal.* **2015**, *5*, 5104.
[29] D. F. Abbott, D. Lebedev, K. Waltar, M. Povia, M. Nachtegaal, E. Fabbri, C. Copéret, T. J. Schmidt, *Chem. Mater.* **2016**, *28*, 6591.
[30] N. Diklic, A. H. Clark, J. Herranz, D. Aegerter, J. S. Diercks, A. Beard, V. A: Saveleva, P. Chauhan, M. Nachtegaal, T. Huthwelker, D. Ledevev, P. Kayser, J. A. Alonso, C. Copéret, T. J. Schmidt, *ACS. Catal.* **2023**, *13*, 11069.
[31] M. Povia, D. F. Abbott, J. Herranz, A. Heinritz, D. Lebedev, B. J. Kim, E. Fabbri, A. patru, J. Kohlbrecher, R. Schäublin, M. Nachtegaal, C. Copéret, T. J. Schmidt, *Energy Environ. Sci.* **2019**, *12*, 3038.
[32] H. N. Nong, T. Reier, H. S. Oh, M. Gliech, P. Paciok, T. H. T. Vu, D. teschener, M. Heggen, V. Petkov, R. Schlögl, T. Jones, P. Strasser, *Nat. Catal.* **2018**, *1*, 841.
[33] S. Roychoudhury, R. Qiao, Z. Zhuo, Q. Li, Y. Lyu, J. H. Kim, W. Yang, *Ener. Environ. Mat.* **2021**, *4*, 246.
[34] W. Yang, T. P. Devereaux, *J. Pow. Sour.* **2018**, *389*, 188.
[35] D. Opalka, C. Scheurer, K. Reuter, *ACS Cat.* **2019**, *9*, 4944.
[36] S. A. C. Carabineiro, F. M. F. De Groot, L. Kjeldgaard, J.-E. Rubensson, B. E. Nieuwenhuys, *Surf. Rew. Lett.* **2004**, *11*, 385.
[37] R. Ruus, A. Saar, J. aark, A. Aidla, T. Uustare, A. Kikas, *J. Elec. Spec. Rel. Phenom.* **1998**, *93*, 193.
[38] Y. Tezuka, S. Shin, T. Uozumi, A. Kotani, *J. Phys. Soc. Jpn.* **1997**, *66*, 3153.
[39] J. Haerberle, M. Richter, Z. Galazka, C. Janowitz, D. Schmeisser, *Thin Solid Films* **2014**, *555*, 53.
[40] M. Michling, D. Schmeisser, *IOP Conf. Ser.: Mater. Sci. Eng.* **2012**, *32*, 012002.
[41] L. J. Falling, R. V. Mom, L. E. Sandoval Diaz, S. Nakhaie, E. Stotz, D. Ivanov, J. J. Velasco-Vélez, *ACS Appl. Mater. Interfaces* **2020**, *12*, 37680.
[42] A. Knop-Gericke, V. Pfeifer, J. J. Velasco-Vélez, T. Jones, R. Arrigo, M. Hävecker, R. Schlögl, *J. Elec. Spec. Rel. Phenom.* **2017**, *221*, 10.

[43] A. Klyushin, R. Arrigo, V. Pfeifer, T. Jones, J. J. Velasco Vélez, A. Knop-Gericke, In *Encyclopedia of Interfacial Chemistry*, Elsevier, Amsterdam **2018**, p. 615.
[44] C. H. Chuang, J. Guo, J. J. V. Vélez, In *Encyclopedia of Solid-Liquid Interfaces*, Elsevier, Amsterdam **2024**, p. 173.
[45] P. Giannozzi, S. Baroni, N. Bonini, *J. Phys.-Condens. Mat* **2009**, *21*, 395502.
[46] P. Giannozzi, O. Andreussi, T. Brumme, *J. Phys.-Condens. Mat.* **2017**, *29*, 465901.
[47] J. P. Perdew, K. Burke, M. Ernzerhof, *Phys. Rev. Lett.* **1996**, *77*, 3865.
[48] A. Dal Corso, *Comp. Mater. Sci.* **2014**, *95*, 337.
[49] E. L. Shirley, *J. Electron. Spectrosc.* **2004**, *136*, 77.
[50] J. A. Soininen, E. L. Shirley, *Phys. Rev. B* **2001**, *64*, 165112.
[51] J. Vinson, J. J. Rehr, J. J. Kas, E. L. Shirley, *Phys. Rev. B* **2011**, *83*, 115106.
[52] E. Pehlke, M. Scheffler, *Phys. Rev. Lett.* **1993**, *71*, 2338.
[53] R. Kraus, V. Bisogni, L. Harnagea, S. Aswartham, S. Wurmehl, G. Levy, I. S. Elfimov, B. Büchner, G. A. Sawatzky, J. Geck, *Phys. Rev. B* **2013**, *87*, 134516.
[54] T. Binninger, M. L. Doublet, *Ener. Environ. Sci.* **2022**, *15*, 2519.
[55] K. H. Saeed, M. Forster, J. F. Li, L. J. Hardwick, A. J. Cowan, *Chem. Commun.* **2020**, *56*, 1129.